

# Synchrotron-based multiple-beam FTIR chemical imaging of a multi-layered polymer in transmission and reflection: towards cultural heritage applications

Miriam Unger · Eric Mattson · Catherine Schmidt  
Patterson · Zahrasadet Alavi · David Carson ·  
Carol J. Hirschmugl

Received: 9 August 2012 / Accepted: 26 November 2012 / Published online: 11 December 2012  
© Springer-Verlag Berlin Heidelberg 2012

**Abstract** IRENI (infrared environmental imaging) is a recently commissioned Fourier transform infrared (FTIR) chemical imaging beamline at the Synchrotron Radiation Center in Madison, WI, USA. This novel beamline extracts 320 mrad of radiation, horizontally, from one bending magnet. The optical transport separates and recombines the beam into 12 parallel collimated beams to illuminate a commercial FTIR microspectrometer (Bruker Hyperion 3000) equipped with a focal plane array detector where single pixels in the detector image a projected sample area of either  $0.54 \times 0.54 \mu\text{m}^2$  or  $2 \times 2 \mu\text{m}^2$ , depending in the measurement geometry. The 12 beams are partially overlapped and defocused, similar to wide-field microscopy, homogeneously illuminating a relatively large sample area compared to single-beam arrangements. Both transmission and reflection geometries are used to examine a model cross section from a layered polymer material. The compromises for sample preparation and measurement strategies are discussed, and the chemical composition and spatial definition of the layers are distinguished in chemical images generated from data sets. Deconvolution methods that may allow more detailed data analysis are also discussed.

## 1 Introduction

Synchrotron-based multiple-beam Fourier transform infrared (FTIR) chemical imaging has recently been developed at the Synchrotron Radiation Center in Madison, WI, USA [1, 2]. Figure 1 shows an overview of the beamline optics. There are two main components of the beamline dedicated to this experimental technique, called IRENI (infrared environmental imaging) that distinguish it from previous synchrotron-based IR beamlines [3]. The first unique component of the beamline is the large swath of radiation that has been collected (Fig. 1, blue arrow), divided, re-focused, collimated and combined into a  $3 \times 4$  beam array to create homogeneous wide-field illumination at the microscope sample plane (Fig. 1b). This differs from traditional synchrotron-based FTIR, which extracts a smaller cone of radiation, and typically illuminates a small sample area. In the IRENI setup, the magnification and numerical aperture (NA) of the microscope objectives define the illuminated area and effective geometric pixel size at the sample plane. Different objectives are employed for transmission and reflection geometries to maximally illuminate the sample plane and minimize the pixel size. The second, critical component of the beamline is a focal plane array detector (Fig. 1, circle) based on HgCdTe detectors (16384 pixels, each  $40 \times 40 \mu\text{m}^2$  area) that collect spectra simultaneously, retaining spatial definition to enable high-resolution imaging of the relatively large illuminated area. FTIR microscopy is routinely applied in the field of cultural heritage research, and advancements in attenuated total reflection (ATR) FTIR [4–6], synchrotron-based FTIR [6–17] and FTIR mapping and imaging [5, 7, 17–22] are improving the information that can be gleaned from samples from works of art. In this context, the unique nature of the IRENI beamline may be well adapted to the identification of materials

M. Unger · E. Mattson · C.J. Hirschmugl (✉)  
Department of Physics, University of Wisconsin-Milwaukee,  
1900 East Kenwood Blvd., Milwaukee, WI 53211, USA  
e-mail: [cjhirsch@uwm.edu](mailto:cjhirsch@uwm.edu)

C. Schmidt Patterson · D. Carson  
Getty Conservation Institute, 1200 Getty Center Drive, Suite 700,  
Los Angeles, CA 90049-1684, USA

Z. Alavi  
College of Engineering and Applied Science, University of  
Wisconsin-Milwaukee, 2200 East Kenwood Blvd., Milwaukee,  
WI 53211, USA

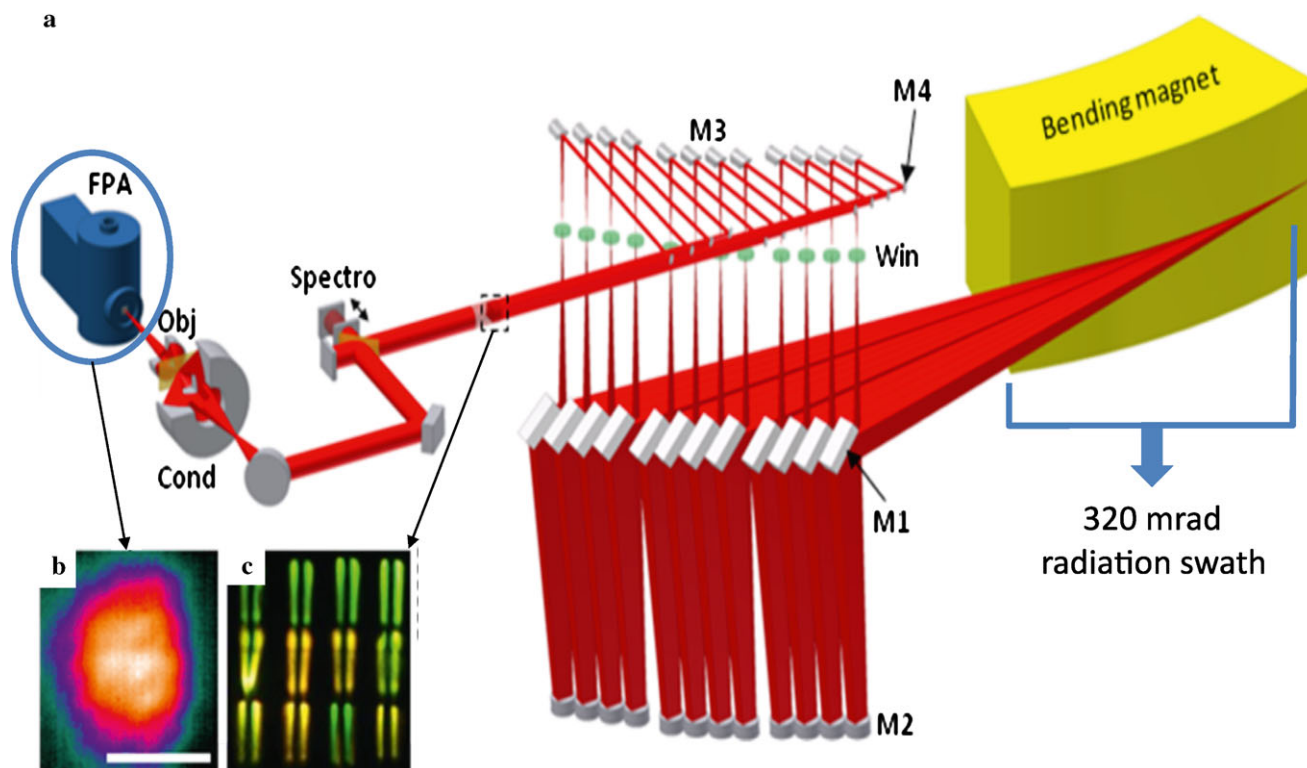


**Fig. 1** (a) IRENI beamline overview:  $M1$ – $M4$  are mirror sets which divide and then re-collimate the synchrotron radiation prior to entering the FTIR spectrometer and associated optics (labeled spectro, cond and obj). *Inset (b)* shows a  $128 \times 128$  pixel FPA (Focal Plane Array) image in which the 12 beams have been overlapped to illuminate an area of

$\sim 50 \mu\text{m} \times 50 \mu\text{m}$ . Scale bar,  $40 \mu\text{m}$ . *Inset (c)* shows a visible-light photograph of the 12 individual beams projected on a screen in the beam path. Scale bar,  $\sim 1.5 \text{ cm}$ . Each beam exhibits a shadow cast by a cooling tube upstream (not shown). (This figure has been reproduced with permission from Ref. [1]. Copyright 2011 Nature Publishing Group)

in such samples, where thin layers of organic material are common.

At IRENI, FTIR data is collected as a hyperspectral cube ( $x, y, \text{Abs}(\nu)$ ), which convolutes the sample information with the point spread function (PSF) of the instrument. This can generate blurry images and, concurrently, contaminated spectra due to the spatial overlap from diffraction. A deconvolution approach to remove the PSF has been described in detail in a recent publication [23], and improves spatial and spectral fidelity of the data sets for a well-known test sample. In brief, Fourier transform based image deconvolution methods have been developed based on the measured and simulated PSFs of a  $2\text{-}\mu\text{m}$  pinhole located at the sample plane. The simulated PSFs are based on the Schwarzschild optic geometry that is modeled as an annulus, since this is the dominating influence in the optical path. The achievable resolution is dependent on wavelength, the NA of the objective and the effective geometric pixel oversampling. The NA plays a similar role as for the Rayleigh criterion, where the ability to resolve two objects is dependent upon wavelength; for the Airy disk the PSF is  $d = 1.22\lambda/\text{NA}$  [24]. There is no similar closed relationship for the Schwarzschild objective [23, 25]. The effective geometric pixel oversampling deter-

mines the ability to achieve the contrast criterion with original data, while deconvolution algorithms are demonstrated to remove the instrumental broadening, and retrieve more faithful images, and thus spectra. In practice, the instrumental broadening is deconvoluted from each image independently, as a function of wavelength, and is subsequently rescaled by requiring equal transmitted light in the original and processed data. Finally, the images are reassembled in a hyperspectral cube. The successful set of parameters for the deconvolution algorithm was determined through evaluation of the spectra and images that were generated from this approach. The resulting algorithm can now be applied to data sets, such as those from the cross-section samples examined in this work, that have been collected with previously evaluated objectives.

In this paper we will show chemical imaging results for a layered polymer material. Synthetic polymers are common components of many objects of modern art and contemporary cultural heritage, including sculptural objects, architectural models, film and animation cells, and coatings. Many polymers found in works of art experience deterioration such as embrittlement and cracking, warping or other deformation, discoloration or becoming increasingly tacky [26].

**Table 1** Optics and scanning parameters employed in this work

Experimental geometry	Condenser	Illuminated area ( $\mu\text{m}^2$ )	Objective	Projected sample area/pixel ( $\mu\text{m}^2$ )	Material used for background measurement	Scans acquired	Time per tile (min)	Area examined ( $\mu\text{m}$ )	Total experimental time (h)
Transmission	15 × (NA 0.58)	34 × 34	74 × (NA 0.6)	0.54 × 0.54	BaF <sub>2</sub>	128	4.5	34 × 204	<0.5
Reflection	N/A	28 × 28	20 × (NA 0.6)	2.00 × 2.00	Au	128	4.5	56 × 112	>1 <sup>a</sup>

<sup>a</sup> Data acquisition required ~0.5 h for the sample, and an additional 0.5 h to collect an appropriate background on a reflective gold slide for background correction

The sample used in this work may be taken as a surrogate for the polymer materials used in modern cultural heritage objects. The composite nature additionally makes it a simple model for the complex layered systems frequently encountered in samples from other cultural heritage materials such as paintings and polychrome sculpture. Importantly, however, the individual layers in the layered polymer are discrete, contain only one chemical component and are organic in nature. This degree of homogeneity is not expected to be present in samples from, for example, a painting, but allows accurate assessment of the IRENI system, demonstrating chemical separation and identification in both transmission and reflection measurement geometries. The results highlight the capabilities and compromises in both geometries, and the results from deconvolution methods that have been applied to the data to remove blurring at the edges due to diffraction are shown. These data, therefore, are expected to inform the application of the IRENI system to more complex and heterogeneous cultural heritage samples, particularly cross sections that contain one or more organic layers/components.

## 2 Materials and methods

The sample examined to assess and demonstrate the ability of the IRENI system to achieve spatially resolved identification of thin layers of organic material was an oxygen barrier film (FR-7750, Bell Fibre Products), which was used as acquired. The oxygen barrier film is a composite material that contains layers of polyester, low-density polyethylene (PE) and chlorotrifluoroethylene (CTFE) [27]. Using the approach commonly employed in cultural heritage science, the sample was cut from the bulk and prepared as a cross section: the removed piece of film was mounted in Bio-Plastic<sup>®</sup> liquid casting plastic (Ward's Natural Science), cured using about one-half the recommended catalyst volume and cut to expose the sample's stratigraphy using an ultramicrotome (PowerTome XL, RMC Products) fitted with a diamond knife (Ultra 45°, Di-ATOME). For reflection experiments, the block face sample was examined. For transmission experiments, a ~3- $\mu\text{m}$ -

thick microtome slice was cut from the block face and retained.

The optics and scanning parameters for the work presented here in transmission and reflection geometries are given in Table 1. A comparison with laboratory-based measurements has been explored in another recent publication [28]. We determined that a sampling area was sufficient when we were able to clearly detect the transitions between each layer in chemical images that were the same shapes as in the visible image. It should be noted that in reflection only one objective is used to both illuminate the sample and couple reflected light to the detector. The objective is therefore maintained in a focused geometry, and the illumination is not homogenized, remaining in the configuration illustrated in Fig. 1, inset (c). Since only one objective is employed, one must compromise on the degree of homogeneity of illumination at the sample, on the degree of magnification or both. In the present case, we both illuminated a smaller part of the sample and collected a larger effective geometric pixel size in reflection than in transmission. In reflection experiments, a half-mirrored beam splitter is employed both before and after the objective to maintain high spatial definition in both directions [29].

To generate absorbance results that are linear with sample concentration, a background of source signal,  $I_0$ , is always collected immediately prior to the sample measurement,  $I_s$ . The absorbance is  $\text{Abs} = -\ln(I_s/I_0)$ . For transmission, the background is taken with no sample in place, and the chemical images are created using a straight-line background in the absorbance spectrum and integrating all intensity between the two baseline frequencies for each material: 1180–1221  $\text{cm}^{-1}$  (CTFE), 2829–2866  $\text{cm}^{-1}$  (PE), 1335–1352  $\text{cm}^{-1}$  (polyester) and 1053–1090  $\text{cm}^{-1}$  (polyester mounting resin). For reflection, a background is collected from gold to detect the maximal signal from the source. Since reflection bands are derivative-like, a Kramers–Kronig (KK) correction is applied to the data [30]. Different integration windows from those used for the transmission data are selected, with straight baselines between two end points: polyester mounting resin 1043–1078  $\text{cm}^{-1}$ ; CTFE 1162–1210  $\text{cm}^{-1}$ , and 1103–1141  $\text{cm}^{-1}$ ; PE 2834–2857  $\text{cm}^{-1}$ ; polyester 1325–1352  $\text{cm}^{-1}$  and 1179–1289  $\text{cm}^{-1}$ .

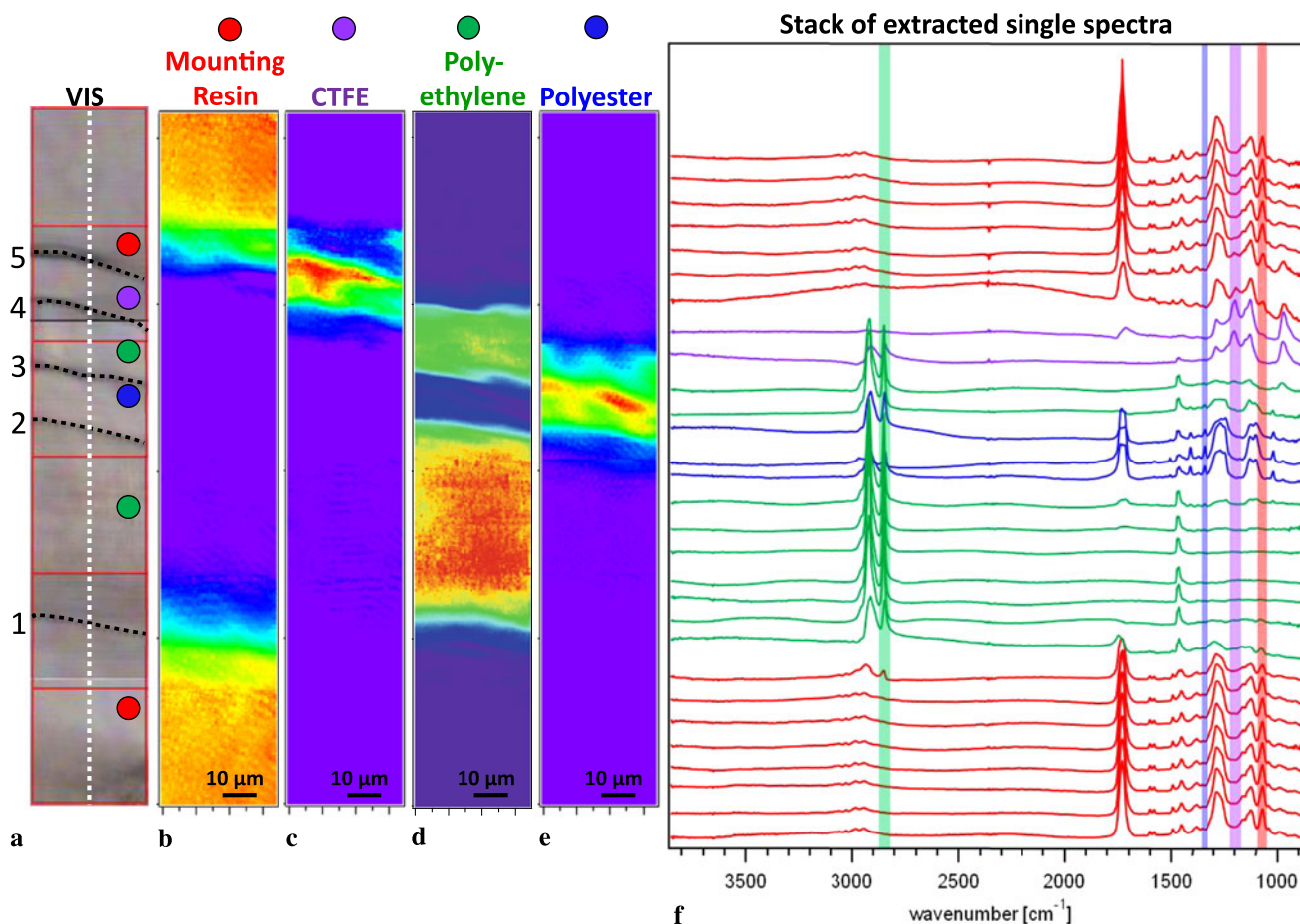


**Fig. 2** Visible (a) and chemical images (b–e) of the layered polymer sample, prepared as a  $\sim 3 \mu\text{s}$  thin section and measured with IRENI in transmission. The layers are described in the text and color coded (red, purple, blue and green for the mounting polyester resin, CTFE, polyester and polyethylene, respectively) to correspond to the spectra at right (f); boundaries between layers are denoted with dashed black

lines and labeled in the visible image at far left. Chemical images are generated from raw data, based on the peak positions highlighted in the stack of spectra at right. The integration ranges are (c)  $1180\text{--}1221 \text{ cm}^{-1}$  (CTFE); (d)  $2829\text{--}2866 \text{ cm}^{-1}$  (PE); (e)  $1335\text{--}1352 \text{ cm}^{-1}$  (polyester) and (b)  $1053\text{--}1090 \text{ cm}^{-1}$  (polyester mounting resin)

### 3 Results and discussion

#### 3.1 Transmission

Figure 2a shows a visible image of the layered sample—with the layers ordered CTFE, PE, polyester and PE, from top to bottom, bounded above and below by the polyester mounting resin—with four chemical images (Fig. 2b–e) resulting from the transmission experiment described above. A stack of spectra (Fig. 2f) is extracted from individual pixels along the center of the image (from the position of the dashed white line in the visible image). The spectra are color coded to represent the majority component in each spectrum (red, purple, blue and green for the mounting polyester resin, CTFE, polyester and polyethylene, respectively). The spectral bands used to create chemical images are defined in Sect. 2 above, and use a rainbow color scale (purple/red for low/high integrated intensity). Each image is

independently scaled, since the signal intensity of the selected marker peaks is distinct for each chemical species in the sample. The images therefore provide a means to visualize the individual layers and faithfully reproduce the structure that is obvious in the visible image. The single-pixel spectra are of sufficient quality to reveal the distinctive chemical signatures for each layer. Indeed, many fewer scans may be used to produce data to distinguish the layers [28].

#### 3.2 Deconvolution

The data used to create the images in Fig. 2 is convoluted with the instrument's PSF. Applying deconvolution algorithms is expected to improve image fidelity and, when scaled properly, the spectral purity. This is desirable if, for example, the goal of an experiment is to determine whether or not layers in a cross section from a painting or other work



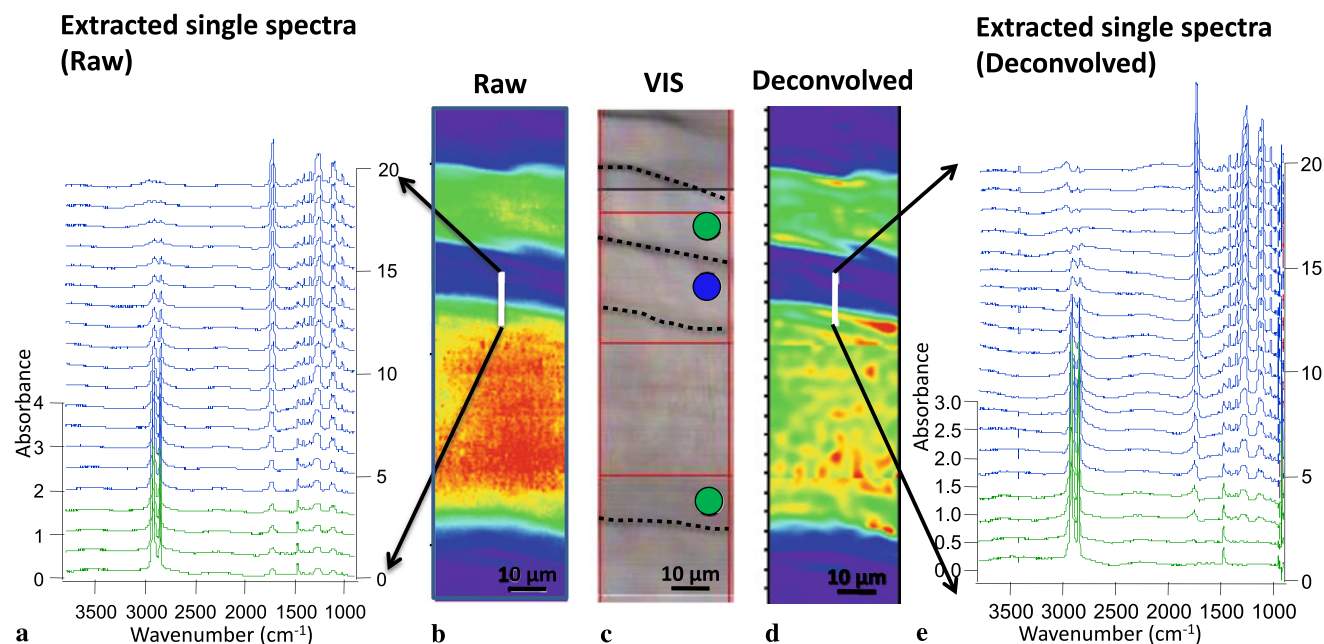


**Fig. 3** Raw and deconvolved chemical images for PE layers (measured in transmission); coding in images is as in Fig. 2. Extracted single spectra from the original (*left-hand side*) and deconvolved data sets (*right-hand side*) taken along the white line in the respective images

of art overlap. Until recently, little progress was made toward deconvolution of IR data in hyperspectral cubes over the entire mid-IR spectral range. Some workers [11] applied Fourier self deconvolution (FSD) to the spatial domain as a means to improve contrast in IR images. This approach, however, deconvolutes a Lorentzian function from the image that is chosen arbitrarily by the user, and may thus lead to images that are not faithful to the original data. This approach is subjective and does not use actual instrumental PSFs. We have recently developed a method for PSF deconvolution using measured PSFs that eliminates the user subjectivity [6]. In our approach, we directly deconvolve PSFs that have been extensively characterized for the Bruker Hyperion 3000 microscope using a conventional Fourier filtering approach over the entire mid-IR region. This approach, in contrast to FSD, removes only the known response function of the system.

Figures 3b and d show chemical images for the original and deconvoluted data, respectively, including the two PE layers of the sample. Two spectral stacks (original (Fig. 3a) and deconvolved (Fig. 3e)) show data from 20 sequential pixels at the second boundary between PE and polyester (the same pixels for both stacks). The spectra before and after deconvolution look similar. The most obvious changes are the intensities for the strongest absorption bands, and upon closer inspection similar impacts across the full spectral range are seen. For example, compare the intensity of the CH stretches ( $2800\text{--}2900\text{ cm}^{-1}$ ) for polyethylene before and after deconvolution for the upper 10 spectra: the absorption intensity decay of the peaks is more rapid after deconvolution.

A similar effect is observed in the bottom 10 spectra for the polyester specific absorption band for the CO functional group ( $1700\text{ cm}^{-1}$ ). The image and stack of data after deconvolution show a sharper boundary and more pure spectral components closer to the transition than in the original data. Deconvolution processes may be important for interpreting data sets from samples with more complex stratigraphy, and less homogeneous layers of unknown composition, such as the samples commonly encountered in cultural heritage research.

### 3.3 Reflection

While transmission geometry is preferred for FTIR imaging to obtain the highest spatial resolution and highest sensitivity due to maximal light throughput, it is not always possible to prepare transmission samples from cultural heritage objects: the ability to prepare thin sections is dependent on the mounting resin, and the porosity, friability, degree of heterogeneity and relative hardness of different layers of the sample under consideration. For example, the soft polymer material used in this sample is amenable to microtoming, while a brittle sample from an aged painting is more difficult to cut into thin sections, particularly when it contains layers of mineral pigments in addition to organic compounds. Here we describe the feasibility and limitations of acquiring chemical images comparable to those presented above without the need to prepare a transmission sample. Figure 4a shows an area of the reserved resin-mounted block face of the same layered organic film sam-

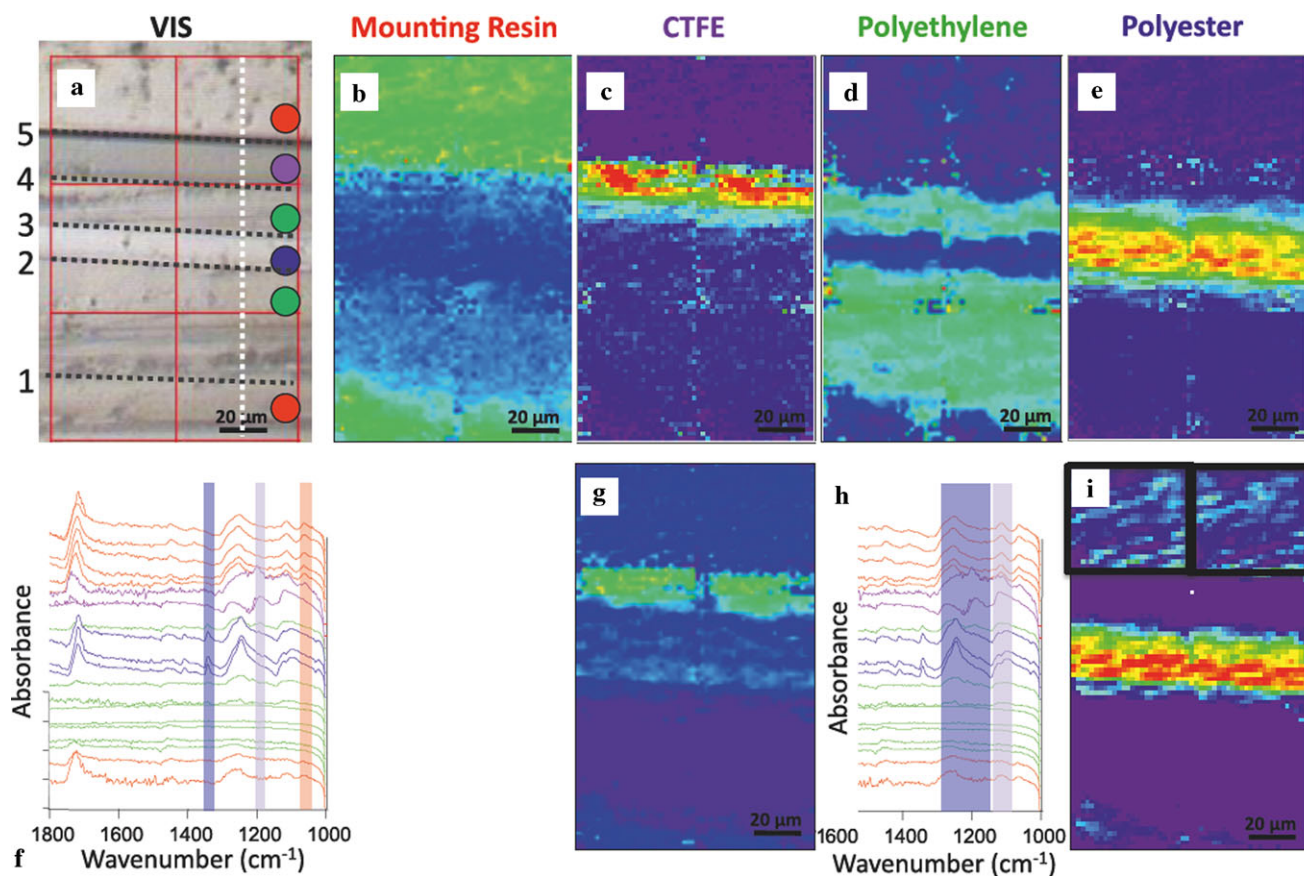


**Fig. 4** Visible image (a) of a cross section of the same layered polymer as shown in Fig. 2, measured with IRENI in reflection. Coding in images is as in Fig. 2. The chemical images (b–e, g and i) are generated from KK-corrected data, based on the highlighted regions in the two stacks of spectra plots (f and h) with the following spectral

windows: polyester mounting resin (b) 1043–1078  $\text{cm}^{-1}$ ; CTFE (c) 1162–1210  $\text{cm}^{-1}$  (upper image) and (g) 1103–1141  $\text{cm}^{-1}$  (lower image); PE (d) 2834–2857  $\text{cm}^{-1}$ ; polyester (e) 1325–1352  $\text{cm}^{-1}$  (upper image) and (i) 1179–1289  $\text{cm}^{-1}$  (lower image)

ple as was shown in Fig. 2a, now measured in reflection mode, and six chemical images for the component layers, one image of the mounting resin (Fig. 4b), one of the PE layers (Fig. 4d) and two images each of the CTFE (Fig. 4c and g) and polyester layers (Fig. 4e and i). Figure 4f and h show stacks of KK-corrected spectra for single pixels across the sample (from the position of the dashed white line in Fig. 4a). Comparing the signal to noise of the reflection (Fig. 4f and h) and transmission (Fig. 2f) spectra, it is clear that the former spectra have a lower signal to noise, as expected, since the signal intensity is reduced due to the IR beam splitter before and after the objective in the optical path. This can be confirmed by calculating the peak-to-peak noise for average spectra of the total measured area for the transmission and reflection data for 1900–2000  $\text{cm}^{-1}$ . The noise is about  $\sim 2.5$  times higher for reflection as compared to transmission. If greater signal to noise is required for a specific analysis, the number of scans can, of course, be increased, impacting the time required for the total measurement.

### 3.4 Impact of Kramers–Kronig analysis

Selecting integration windows to generate chemical images is more challenging for reflection data, in general, than for transmission data, since both raw and KK-corrected reflection spectra have broader features than transmission data [30]. In reflection, the real part of the index of refraction is detected as a derivative-type feature for each absorption band with broader spectral content than the corresponding transmission absorption band. KK transforms for narrow spectral regions (here 2000  $\text{cm}^{-1}$  as opposed to at least 10 000  $\text{cm}^{-1}$ ) inherently retrieve absorption spectra that retain derivative-like features with more spectral overlap than the corresponding transmission absorption bands. A potential impact is demonstrated in chemical images in Fig. 4. In particular, the mounting resin chemical image (Fig. 4b) shows subtle variations (in blue) in the central portion of the image, suggesting the presence of varying low-intensity features of the embedding medium within the confines of the sample. The selected integration parameters for the mounting resin overlap with structure in all of the spectra as seen in

the stack of spectra in Fig. 4f. Similar artifacts are apparent in the images and spectra for both the CTFE and polyester absorption bands. Unfortunately, such overlaps are difficult to avoid in relevant cultural heritage samples, which tend to have complex FTIR spectra with many overlapping features.

Another artifact that can sometimes be observed in images derived from reflection measurements is beam structure that is most prominently seen in the chemical image at the bottom right in Fig. 4i (in black boxes) as co-located with the mounting resin. The color variation in the chemical image for the top two tiles of the image shows a similar underlying structure. This is typically apparent only for weak spectral features in reflection spectra as in this case. Here, the spectral feature for the resin (at  $\sim 1240\text{ cm}^{-1}$ ) overlaps with the broad polyester band ( $1178\text{--}1289\text{ cm}^{-1}$ ). Comparing the chemical images for the CTFE (Fig. 4c and g) and polyester layers (Fig. 4e and i) makes it clear that the selection of integration windows impacts the degree to which beam structure is present in the resulting image: the images in the top row show less beam structure than the images in the bottom row, and utilize slightly different integration windows.

The artifact is due to the 12 separated beams that are necessarily in focus at the sample plane, since there is no condenser to defocus and homogenize the illuminated beam pattern. The signal variation across the beam structure encompasses approximately two orders of magnitude of difference in intensity across the field of view. The background (reference) measurement is collected from a gold mirror that is typically independent from the plastic-embedded sample. To retain perfect alignment, we calculate that the reflection

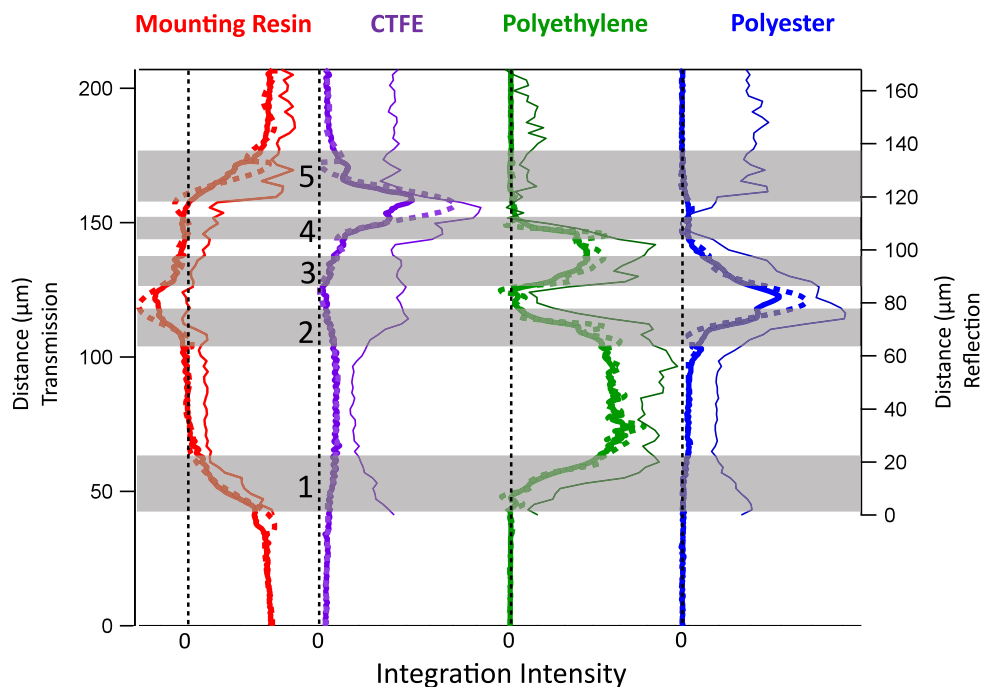
angle for both the reference and sample would need to be accurate to within 0.2 mrad, resulting in a source intensity shift of less than one pixel. That is challenging to achieve for two separate objects and it is inevitable to retain a small signal from the beam structure in the resulting image, especially for weak absorption features. If reflection is the optimal measurement for the system, we recommend evaporating gold on the embedding medium to act as a reference surface by reducing the alignment challenges. However, one must take care that the gold can be adequately applied such that it does not delaminate and the process does not damage the sample of interest.

Alternatively, one can choose a higher magnification objective for reflection geometry to further homogenize the beams. This would reduce the projected sample area at each detector pixel, leading to a more strict requirement on sample alignment and reduce available signal, requiring longer measurement times. The presence of artifacts such as these in reflection data means that the chemical images and the individual spectral curves from which they are derived—both before and after spectral correction—must be examined closely to accurately analyze data from FTIR imaging experiments performed in reflection.

### 3.5 Comparison between transmission, deconvolution and reflection results

We now compare the data in Figs. 2–4 by extracting line scans that are shown together in Fig. 5 (from the positions of the white dashed lines in Figs. 2a and 4a), where transmission and reflection results are represented by thick solid

**Fig. 5** Vertical line scans from chemical images for reflection measurements (*thin solid lines, right-hand axis*), raw transmission measurements (*thick solid lines, left-hand axis*) and deconvoluted transmission data (*dashed lines, left-hand axis*). The boundaries are highlighted in grey and labeled as in Fig. 2. The integration windows used are: mounting resin  $1043\text{--}1078\text{ cm}^{-1}$  (refl.) and  $1053\text{--}1090\text{ cm}^{-1}$  (trans.); CTFE  $1103\text{--}1141\text{ cm}^{-1}$  (refl.) and  $1180\text{--}1221\text{ cm}^{-1}$  (trans.); polyethylene  $2834\text{--}2857\text{ cm}^{-1}$  (refl.) and  $2829\text{--}2866\text{ cm}^{-1}$  (trans.); polyester  $1179\text{--}1289\text{ cm}^{-1}$  (refl.) and  $1335\text{--}1352\text{ cm}^{-1}$  (trans.)





and thin solid traces, respectively. While a similar sample was measured by both methods, the unique sample preparation for transmission (cross section) and reflection (embedded in resin) requires that we have measured two distinct sections of the sample. The line scans have been offset to match the boundaries that have been labeled for clarity. The length scale is dictated by the magnification of the objective and therefore the projected sample size on a detector pixel. No further scaling beyond choosing an offset has been implemented. Line scans from chemical images derived after applying deconvolution algorithms to the transmission data are also included (dashed traces). Comparing the line scans from the KK-corrected reflection data, and both the raw and deconvolved transmission data, similar trends are observed. The parallel slopes for boundaries 1–4 indicate that the data are showing the same trends at the boundaries, underscoring the notion that either experimental geometry may be employed.

While overall the line scan shapes are similar, there exists a notable exception: at boundary 5 (the edge between CTFE and mounting resin) the change in the intensity of the mounting resin (red traces) appears sharper in reflection geometry than in transmission. This apparent difference is of interest since in the analysis of cross-section samples, boundaries are significant: a sharp transition may indicate a wet-on-dry paint application, while a more gradual transition may imply a wet-on-wet paint application. A complete understanding of the edges between layers therefore may allow an evaluation of artists' technique in samples from painting cross sections.

Importantly, transmission spectra are representative of the entire thickness of the sample, while the reflection spectra are representative of different thicknesses of material, depending on the indices of refraction encountered at each wavelength, which can impact the penetration depth of the reflected radiation, and consequently the derived images/line scans. Such considerations are magnified if the sample itself is not introduced normal to the incoming radiation, a configuration more easily achieved with the substantial block face sample than with the delicate transmission thin section. The sample itself may also, of course, impact the observed boundary. Broad boundaries may represent actual mixing of two constituents at that interface, or may be an artifact of, for example, a loss of sample integrity in a thin transmission sample, where surface curvature (introduced during the microtoming process) can create physical separation between the layers, marring the boundaries between materials as compared to the block face sample. Furthermore, the IR images are a 2D projection of the sample, and curvature will itself impact the sharpness of boundaries observed in chemical images. Each of these factors must be considered in the analysis of boundaries.

Interestingly, the slope of the integrated intensity of the polyester absorption band (blue traces in Fig. 5) appears somewhat lower at boundary 3 than boundary 2, in both the transmission and reflection data. Though the source of this change is not obvious in this particular sample, this observation demonstrates the ability, regardless of experimental geometry, to detect subtle differences between two similar boundaries, a relevant consideration for the analysis of cultural heritage samples.

### 3.6 Effects of data processing

The line scan data shown in Fig. 5 demonstrate the effects of post processing: the data from the deconvolved chemical images typically show sharper edges, with larger maxima and minima at the boundaries independent of the wavelength for the absorption band. The chemical images generated from spectral integration windows must be carefully evaluated, surveying the spectra, images and line scans to gain insight. For example, the negative values in the line scan data for the mounting resin shown on the left of Fig. 5 (red traces, seen as a departure from baseline values around  $80\ \mu\text{m}$  (reflection)/ $120\ \mu\text{m}$  (transmission)) arise from the overlap of a feature of the polyester layer within the sample's layered structure with the integration window used to localize the polyester mounting resin ( $1043\text{--}1078\ \text{cm}^{-1}$ ). That this anomaly stems from a spectral overlap is apparent from the concomitant rise in the same location in the polyester layer (blue traces at right) in Fig. 5. This occurs since the baseline correction to extract the integrated intensity is satisfactory for the mounting resin (and is indeed chosen based on individual spectral curves from that region), but also extracts an unexpected value from other infrared spectra within the data set that have some portion of an overlapping absorption band in the selected spectral region. This is easily seen in the stacks of data in Figs. 2f and 4f. The mounting resin band (highlighted in red) clearly overlaps an edge of a spectral feature for the polyester that is not surprising since both materials are polyester. This leads to the slight deviation from the baseline in the CTFE transmission line scan, and a larger deviation in reflection. The overlapping features with the selected CTFE integration window ( $1180\text{--}1221\ \text{cm}^{-1}$ ) can be seen in the spectra in Figs. 2 and 4.

Additionally, the applying deconvolution can potentially introduce artifacts at sharp discontinuities or interfaces due to the phenomenon of Gibb's ringing. In brief, a Fourier reconstruction of a piecewise-continuous function will lead to an over/undershoot of the intensity values at the discontinuity that will produce decaying oscillations in the vicinity of the discontinuity. Fortunately, such artifacts have a characteristic 'ringing' or 'rippling' appearance that can be easily identified. Since ringing artifacts have a very regular, characteristic pattern of decaying oscillation near a sharp or



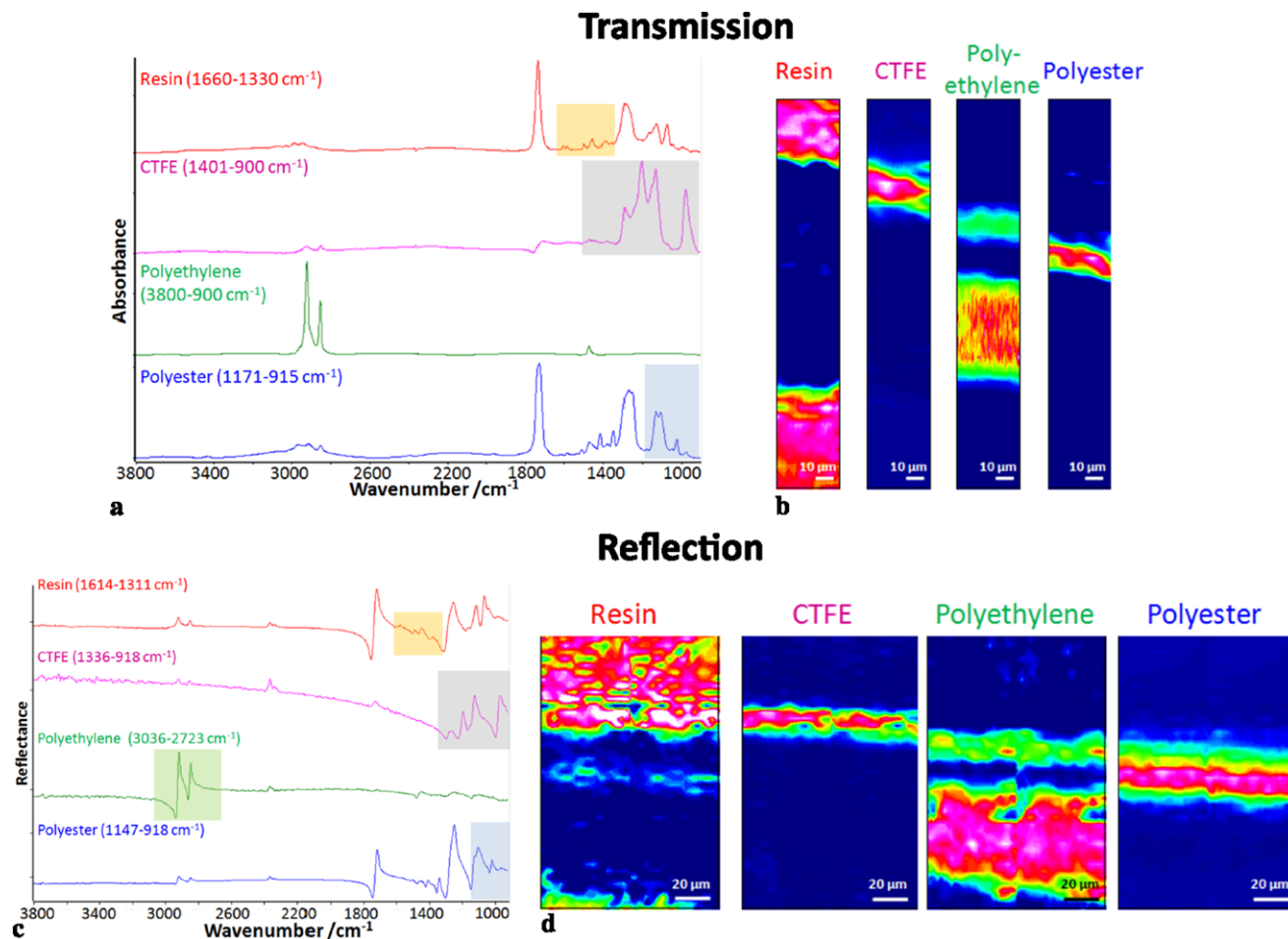


**Fig. 6** Multivariate correlation approach of the transmission (*top*) and reflection (*bottom*) data. *Transmission mode* (*A + B*); (**a**) reference FTIR spectra of each component used for the correlation method, (**b**) FTIR correlation images of mounting resin for 1330–1660  $\text{cm}^{-1}$ , CTFE for 900–1401  $\text{cm}^{-1}$ , polyethylene and polyester for

915–1171  $\text{cm}^{-1}$ . *Reflection mode* (*C + D*); (**c**) reference FTIR spectra of each component, (**d**) FTIR correlation images of resin (1311–1614  $\text{cm}^{-1}$ ), CTFE (918–1346  $\text{cm}^{-1}$ ), PE (2723–3036  $\text{cm}^{-1}$ ) and polyester (918–1147  $\text{cm}^{-1}$ )

abrupt discontinuity or intensity change, the user should expect and be able to identify their presence in real data sets. Thus, while care must be taken to distinguish these artifacts from meaningful information, their identification is straightforward and misinterpretation can be easily circumvented. Such challenges are likely to be present in the analysis of any complex material, and will influence the examination of cross sections from cultural heritage materials that are expected to share features (such as binding medium) between layers in some instances.

### 3.7 Multivariate correlation approach

Alternative analytical methods that rely on information from a larger spectral range can be employed to overcome these limitations as needed, and include correlating standard spectra with each pixel of data, principal component analysis and statistics-based clustering analysis. Here we apply multivariate

correlation analysis. When spectral features are superimposed, for correlation analysis specific spectral regions of the pure components are selected and correlated to all individual pixel spectra within the measured area. This powerful tool can overcome some of the limitations mentioned above and aid analysis of multi-component samples with similar spectral features. The spectral ranges employed for correlation analysis have been highlighted in the standard spectra shown in Figs. 6a and 6c for transmission and reflection, respectively. In Figs. 6b and d the results of multivariate correlation are shown for transmission and reflection, respectively. The correlation images clearly demonstrate the differentiation between each layer (blue/red indicates small/large similarity) and are comparable to the integration images discussed above. However, for reflection data (Figs. 6c and d) the spectral range chosen for the resin correlation image has some degree of similarity with the CTFE spectra, and these layers are not clearly distinguished in the resin-specific im-

age (Fig. 6d). The similarity between the two spectra in Fig. 6c is obvious when comparing the selected spectral region for resin with the CTFE-specific spectrum.

## 4 Conclusion

In sum, a synchrotron-based, multiple-beam FTIR chemical imaging beamline complements existing technologies to provide additional information for measuring samples of interest to the cultural heritage community. The sample presented here demonstrates the ability to chemically separate and identify organic materials in a layered system. However, any chemical species that can be identified by FTIR spectroscopy, including some inorganic pigments and fillers expected in a painting cross section [22], may be analyzed in this fashion and may benefit from the data processing processes described. Sample preparation and experimental approach must both be considered to identify the optimal approach for examining precious samples. Reflection samples can be prepared relatively easily and measured with complementary techniques commonly employed in cultural heritage science. However, a longer measurement time is likely to obtain similar quality measurements covering the same sample area, and compromises are made regarding the optical path to analyze these samples. For the reflection geometry, one objective is used for both illuminating and focusing the beam on the detector, while, for transmission, different objectives can be used. The projected sample area per detector pixel area is determined by the magnification of the focusing objective, while the illumination area is defined by the condensing objective, so the choices made for the optical path components directly influence the spatial resolution of resulting chemical images and the size/area that can be examined in a reasonable period of time. Ideally, the array of synchrotron beams are slightly defocused to illuminate the sample homogeneously, which cannot be employed for reflection measurements since one objective is used for both illumination and focusing the image on the detector, and defocusing would degrade the image quality.

Sample measurements of a layered polymer material show that the sharp and gradual transitions between chemically distinct layers can be detected, and deconvolution improves the quality of the data, showing sharper edges between layers. These results demonstrate that the chemical images and line scans derived from original and deconvoluted data collected at IRENI can reveal the chemical identity and distribution in chemically distinct samples, and may be useful in the characterization of artistic practice in some cases.

**Acknowledgements** This work was supported by the US National Science Foundation under awards CHE-0832298, CHE-1112433 and DMR-0619759, the Research Growth Initiative of the University of

Wisconsin-Milwaukee, and is based on research conducted at the Synchrotron Radiation Center, University of Wisconsin-Madison, which is supported by the National Science Foundation under award DMR-0537588 and by the University of Wisconsin-Milwaukee and the University of Wisconsin-Madison.

## References

1. M.J. Nasse, M.J. Walsh, E.C. Mattson, R. Reininger, A. Kajdacsy-Balla, V. Macias, R. Bhargava, C.J. Hirschmugl, *Nat. Methods* **8**, 413 (2011)
2. M.J. Nasse, E.C. Mattson, R. Reininger, T. Kubala, S. Janowski, Z. El-Bayyari, C.J. Hirschmugl, *Nucl. Instrum. Methods Phys. Res., Sect. A, Accel. Spectrom. Detect. Assoc. Equip.* **649**, 172 (2011)
3. J.A. Reffner, P.A. Martoglio, G.P. Williams, *Rev. Sci. Instrum.* **66**, 1298 (1995)
4. S. Prati, E. Joseph, G. Sciutto, R. Mazzeo, *Acc. Chem. Res.* **43**, 792 (2010)
5. E. Joseph, S. Prati, G. Sciutto, M. Ioele, P. Santopadre, R. Mazzeo, *Anal. Bioanal. Chem.* **396**, 899 (2010)
6. R. Sloggett, C. Kyi, N. Tse, M.J. Tobin, L. Puskar, S.P. Best, *Vib. Spectrosc.* **53**, 77 (2010)
7. J.P. Echard, M. Cotte, E. Dooryhee, L. Bertrand, *Appl. Phys. A* **92**, 77 (2008)
8. G.D. Smith, *J. Am. Inst. Conserv.* **42**, 399 (2003)
9. N. Salvadó, S. Buti, M.J. Tobin, E. Pantos, A. Prag, T. Pradell, *Anal. Chem.* **77**, 3444 (2005)
10. N. Salvadó, S. Buti, E. Pantos, F. Bahrami, A. Labrador, T. Pradell, *Appl. Phys. A* **90**, 67 (2007)
11. M. Cotte, P. Dumas, Y. Taniguchi, E. Checroun, P. Walter, J. Susini, *Phys. Herit.* **10**, 590 (2009)
12. M. Cotte, E. Checroun, V. Mazel, V.A. Solé, P. Richardin, Y. Taniguchi, P. Walter, J. Susini, *e-Preserv. Sci.* **6**, 1 (2009)
13. D. Creagh, A. Lee, V. Otieno-Alego, M. Kubik, *Radiat. Phys. Chem.* **78**, 367 (2009)
14. J.-P. Echard, L. Bertrand, A. von Bohlen, A.-S. Le Hô, C. Paris, L. Bellot-Gurlet, B. Soulier, A. Lattuati-Derieux, S. Thao, L. Robinet, B. Lavédrine, S. Vaiedelich, *Angew. Chem., Int. Ed. Engl.* **49**, 197 (2010)
15. A. Lluveras, S. Boularand, A. Andreotti, M. Vendrell-Saz, *Appl. Phys. A* **99**, 363 (2010)
16. L. Bertrand, L. Robinet, M. Thoury, K. Janssens, S.X. Cohen, S. Schöder, *Appl. Phys. A* **106**, 377 (2012)
17. M. Cotte, E. Checroun, J. Susini, P. Walter, *Appl. Phys. A* **89**, 841 (2007)
18. J. Van der Weerd, H. Brammer, J.J. Boon, R.M.A. Heeren, *Appl. Spectrosc.* **56**, 275 (2002)
19. C. Ricci, S. Bloxham, S.G. Kazarian, *J. Cult. Herit.* **8**, 387 (2007)
20. M. Spring, C. Ricci, D.A. Pegg, S.G. Kazarian, *Anal. Bioanal. Chem.* **392**, 37 (2008)
21. E. Joseph, C. Ricci, S.G. Kazarian, R. Mazzeo, S. Prati, M. Ioele, *Vib. Spectrosc.* **53**, 274 (2010)
22. M.J. Nasse, B. Bellehumeur, S. Ratti, C. Olivieri, D. Buschke, J. Squirrel, K. Eliceiri, B. Ogle, C.S. Patterson, M. Giordano, C.J. Hirschmugl, *Vib. Spectrosc.* **60**, 10 (2012)
23. E.C. Mattson, M.J. Nasse, M. Rak, K.M. Gough, C.J. Hirschmugl, *Anal. Chem.* **84**, 6173 (2012)
24. M. Born, E. Wolf, *Principles of Optics* (Pergamon, New York, 1965)
25. B.J. Davis, P.S. Carney, R. Bhargava, *Anal. Chem.* **82**, 3474 (2010)
26. L. Bertrand, F. Alban, M. Graham, *Preservation of Plastics Artefacts in Museum Collections* (Éditions du Comité des Travaux Historiques et Scientifiques, Paris, 2012)

27. M. Shin, K. Elert, *The Use of Oxygen-Free Environments in the Control of Museum Insect Pests* (The Getty Conservation Institute, Los Angeles, 2003)
28. C.M. Schmidt Patterson, D. Carson, A. Phenix, H. Khanjian, K. Trentelman, J. Mass, C. Hirschmugl, *ePreserv. Sci.* **9** (2012) submitted
29. H. Bechtel, M. Martin, T. May, P. Lerch, *Rev. Sci. Instrum.* **80**, 126106 (2009)
30. P. Griffiths, J.A. De Haseth, *Fourier Transform Infrared Spectrometry*. Chemical Analysis: A Series of Monographs on Analytical Chemistry and Its Applications (Wiley-Interscience, New York, 2007)